

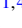




Magnetic and structural dimer networks in layered $\text{K}_2\text{Ni}(\text{MoO}_4)_2$ G. Senthil Murugan ^{1,*}, K. Ramesh Babu ^{2,3}, R. Sankar ^{1,4,†}, W. T. Chen ^{1,5}, I. Panneer Muthuselvam ⁶,
Sumanta Chattopadhyay⁷ and K.-Y. Choi⁸¹Center for Condensed Matter Sciences, National Taiwan University, Taipei 10617, Taiwan²Department of Physics and Center for Theoretical Physics, National Taiwan University, Taipei 10617, Taiwan³Physics Division, National Center for Theoretical Sciences, Hsinchu 30013, Taiwan⁴Institute of Physics, Academia Sinica, Taipei 11529, Taiwan⁵Taiwan Consortium of Emergent Crystalline Materials, Ministry of Science and Technology, Taipei 10622, Taiwan⁶Department of Physics (MMV), Banaras Hindu University, Varanasi 221005, Uttar Pradesh, India⁷Dresden High Magnetic Field Laboratory, Forschungszentrum Dresden-Rossendorf, 01314 Dresden, Germany⁸Department of Physics, Chung-Ang University, Seoul 156-756, Republic of Korea

(Received 8 April 2020; revised 18 January 2021; accepted 21 January 2021; published 29 January 2021)

The magnetic and thermodynamic properties of layered single-crystal $\text{K}_2\text{Ni}(\text{MoO}_4)_2$ having both structural and magnetic dimers have been investigated. The crystal structure of $\text{K}_2\text{Ni}(\text{MoO}_4)_2$ is composed of edge-sharing NiO_6 -octahedral pairs bridged by the MoO_4^{2-} polyatomic ion groups in a plane, and the K^+ ions sit in the van der Waals gap between the layers. The temperature dependence of magnetic susceptibility shows a spin-singlet ground state with an activation gap of $\Delta/k_B \approx 38$ K. A high-field magnetization study at $T = 1.5$ K exhibits a half-magnetization plateau at $\mu_0 H \sim 25$ T, corresponding to a level crossing of the singlet ground state with the lowest triplet state. Further, we have performed density functional theory calculations to determine magnetic exchange interactions. The nearest-neighbor coupling constant $J_1 \sim 10$ K between the Ni spins turns out to be an order of magnitude larger than all interdimer couplings. Our experimental and theoretical results suggest that $\text{K}_2\text{Ni}(\text{MoO}_4)_2$ constitutes a nearly isolated two-dimensional $S = 1$ dimer model.

DOI: [10.1103/PhysRevB.103.024451](https://doi.org/10.1103/PhysRevB.103.024451)**I. INTRODUCTION**

In the past two decades, spin dimer materials have garnered a great deal of attention because a spin gap between the spin-singlet ground state to the excited triplet state exhibits a variety of exotic phenomena such as the realizations of Bose-Einstein condensation (BEC) and the appearance of magnetization plateaus [1–5]. A spin dimerization can occur in spin-Peierls, spin-ladder, and frustrated quantum magnets. The prototypical examples include CuGeO_3 in one dimension (1D) [6] and $\text{SrCu}_2(\text{BO}_3)_2$ in 2D [3].

Besides the spin-gap opening in noninteger spin systems, Haldane conjectured that integer-spin antiferromagnetic (AF) Heisenberg chains can also have an energy gap due to topological origin [7]. Since then, 1D $S = 1$ AF Heisenberg chains have been the subject of intense research. Several quasi-1D $S = 1$ chain systems have been proposed to test the Haldane conjecture, such as CsNiCl_3 [8], Y_2BaNiO_5 [9], $\text{PbNi}_2\text{V}_2\text{O}_8$ [10], and $\text{SrNi}_2\text{V}_2\text{O}_8$ [11]. However, the occurrence of 3D AF ordering in the $T \rightarrow 0$ limit preempts an inherent topological gap opening expected for the integer spins. In real materials, it is extremely challenging to find perfect integer-spin chain compounds, which are free from interchain perturbations. For example, the $S = 1$ spin chain compound CsNiCl_3 has been considered as a model system verifying the Haldane conjecture, yet tiny next-nearest-neighbor coupling constant J' with

an order of $J'/J \sim 1\%$ turns out to be sufficient to stabilize the long-range AF ordering at $T_N \sim 4.8$ K [12]. The interchain coupling detrimental to the Haldane gapped phase obscures the sought-after spin-gap opening.

Noticeably, the $S = 1$ tetramer antiferromagnet $\text{K}_2\text{Ni}_2(\text{MoO}_4)_3$ is found to be located near a quantum critical point, while adjoining a spin-gap phase [13]. This motivates us to search for related spin dimer compounds. We find that $\text{K}_2\text{Ni}(\text{MoO}_4)_2$ is a candidate of a nearly perfect $S = 1$ dimer system on both structural and magnetic aspects. Each layer of $\text{K}_2\text{Ni}(\text{MoO}_4)_2$ is composed of NiO_6 -octahedral pairs bridged by MoO_4 groups with the K^+ ions intercalated between the layers, as shown in Fig. 1. The structural $S = 1$ dimers are formed by edge-shared NiO_6 octahedra. These $S = 1$ dimers are weakly connected through MoO_4 tetrahedral units in the ac layer while being terminated by the van der Waals (vdW) gap.

Through comprehensive thermodynamic characterizations, we determine a spin gap of $\Delta/k_B \approx 38$ K. Herein, details of single-crystal growth, dc and ac magnetic susceptibilities, and specific heat measurements are presented. Supplemented with these thermodynamic data, magnetic exchange interactions calculated with density functional theory demonstrate that $\text{K}_2\text{Ni}(\text{MoO}_4)_2$ realizes an almost isolated two-dimensional $S = 1$ dimer system.

II. EXPERIMENTAL AND CALCULATION DETAILS

A polycrystalline sample of $\text{K}_2\text{Ni}(\text{MoO}_4)_2$ was prepared by the solid-state reaction method using K_2MoO_4 , NiO , and

*Corresponding author: nanosen@gmail.com

†Corresponding author: sankarndf@gmail.com

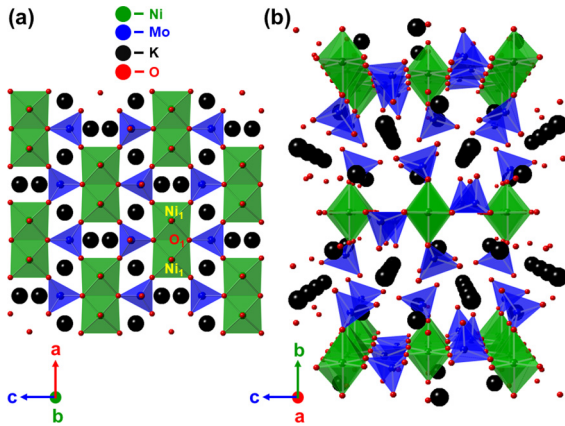


FIG. 1. (a) 2D and (b) 3D view of the crystal structure of $\text{K}_2\text{Ni}(\text{MoO}_4)_2$. The edge-shared NiO_6 octahedral pairs form dimers connected by the polyatomic ion groups of MoO_4^{2-} in the ac plane with the K^+ ions in the van der Waals gaps.

MoO_3 (higher than 99.95% pure) as starting materials. A mixture of the reagents was calcined at 400°C in the air for 48 hours, ground, and sintered at 450°C and 500°C for 48 hours each with intermediate grindings. Platelike single crystals of $\text{K}_2\text{Ni}(\text{MoO}_4)_2$ in yellow-green color have been successfully grown from the mixture of the polycrystalline sample and K_2MoO_4 in the weight ratio of 1:2. The photo of the typical sample of $\sim 3.5 \times 2.2 \times 0.2 \text{ mm}^3$ size is shown in the inset of Fig. 2.

The single-crystal quality and phase purity was confirmed by powder x-ray diffraction (Bruker D2). The synchrotron XRD patterns were obtained with the MYTHEN detector with a 15 keV beam at the 09A beamline of NSRRC in Taiwan. The crushed-crystal sample was packed in a 0.1 mm borosil-

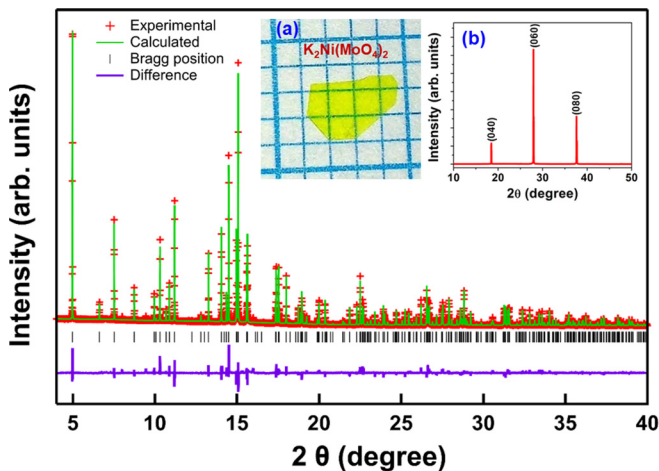


FIG. 2. Rietveld refinement of the synchrotron XRD powder pattern using crushed crystals of $\text{K}_2\text{Ni}(\text{MoO}_4)_2$ taken at room temperature. The observed data, Rietveld refinement fit, Bragg peaks, and difference curve are denoted by the plus sign symbols, green solid line, vertical black dashes, and purple line, respectively. The insets show an image of the as-grown single crystal with the easily cleaved ac plane, and XRD pattern of a cleaved plane which has a preferred orientation of indexed $(0K0)$ peaks.

icate capillary and the capillary was kept spinning during data collection. The collected patterns were analyzed with the Rietveld method using the program of Bruker TOPAS. A neutron powder diffraction experiment has been performed on a powder sample with 7.53 g at beamline Echidna, ANSTO, Australia. The temperature-dependent diffraction patterns were collected in a 9 mm diameter vanadium can with a neutron wavelength of 2.43 \AA . The obtained data were analyzed with the Rietveld method using the program DIFFRAC.TOPAS.

The magnetic measurements were performed using a superconducting quantum interference device vibrating-sample magnetometer (SQUID-VSM, Quantum Design, USA). The high-field magnetization measurements were carried out at the Dresden High Magnetic Field Laboratory in Germany using a pulsed-field magnet. The specific heat data were obtained using a standard relaxation method with a physical property measurement system (PPMS; Quantum Design, USA).

DFT calculations were performed with the generalized gradient approximation (GGA) being taken care of by the Perdew-Burke-Ernzerhof parametrization (PBE) [14]. To describe the electron-electron interactions of $3d$ states of Ni, the GGA with on-site Coulomb repulsion (GGA + U) calculations were performed with an effective U parameter $U_{\text{eff}} = 6 \text{ eV}$ [15]. The accurate projector augmented wave method as implemented in the Vienna *Ab initio* Simulation Package [16–19] was used for the present study. The crystal structure of $\text{K}_2\text{Ni}(\text{MoO}_4)_2$ contains eight formula units per unit cell. All the present calculations were carried out with experimental lattice parameters. The one-electron Kohn-Sham wave functions were expanded in a plane-wave basis set with a cutoff energy of 480 eV. The integrations over the Brillouin zone were performed with a k -point grid of $8 \times 6 \times 4$ by following the Monkhorst-Pack scheme. The convergence criteria for the total energy was set to be 10^{-6} eV .

III. RESULTS AND DISCUSSION

A. Crystal structure

The as-grown single crystal is shown in the inset of Fig. 2 with the as-cleaved plane of preferred $(0K0)$ orientation direction. $\text{K}_2\text{Ni}(\text{MoO}_4)_2$ crystallizes in an orthorhombic crystal structure of space group $Cmca$ (No. 64) as shown in Fig. 1 [20], where layers of edge-sharing NiO_6 -octahedra pairs are bridged by the polyatomic ion groups of MoO_4^{2-} in the ac plane, and the K^+ ions are in the interstitial sites between the dimer layers. Figure 2 shows the synchrotron XRD powder pattern using crushed crystals of $\text{K}_2\text{Ni}(\text{MoO}_4)_2$ at room temperature. The fitted lattice parameters are $a = 8.47618 \pm 0.00005 \text{ \AA}$, $b = 19.0473 \pm 0.0001 \text{ \AA}$, $c = 10.85018 \pm 0.00008 \text{ \AA}$, and $V = 1751.72 \pm 0.02 \text{ \AA}^3$, which are in good agreement with those published in the literature [20]. The goodness of fit is shown by the residual refinement factors of $R_p = 4.82\%$, $R_{\text{wp}} = 7.33\%$, $R_{\text{exp}} = 1.69\%$, and $\chi^2 = 4.33$.

The temperature evolution of the lattice parameters was derived from the Rietveld refinement of the obtained neutron powder diffraction data between 2–200 K, and synchrotron XRD at 300 K. The results are summarized in Figs. 3(a)–3(c), where the error bars are smaller than the symbol size. The

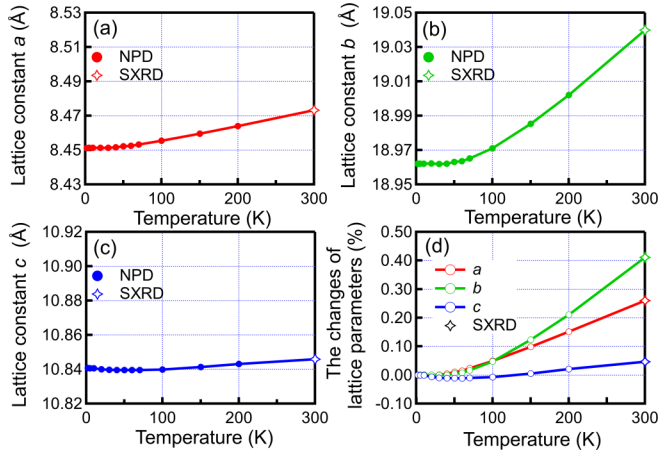


FIG. 3. The refined lattice constants are analyzed from the neutron powder diffraction data between 2 and 200 K. (a), (b), and (c) are the temperature evolution of the lattice parameters a , b , and c , respectively, where the scale of y axes is set to be the same for comparison. The 300 K data are derived from synchrotron XRD refinement results. (d) Change of the lattice parameters is plotted as a percentage against the base temperature lattice parameters.

temperature dependence of the lattice constants follows the typical linear thermal expansion with increasing temperature between 38 and 300 K. As seen from the relative change of the lattice parameters in Fig. 3(d), the thermal expansion is anisotropic. This is consistent with the fact that the most significant change occurs in the b axis due to dipole contribution across the vdW gap. The refined structural parameters of $\text{K}_2\text{Ni}(\text{MoO}_4)_2$ at $T = 300$ K (synchrotron XRD) and $T = 2$ K (neutron powder diffraction patterns) are summarized in Table I.

B. Static magnetic susceptibility

Figure 4 shows the temperature dependence of dc magnetic susceptibilities $\chi = M/H$ for the $\text{K}_2\text{Ni}(\text{MoO}_4)_2$ powder sample measured in an applied field of $\mu_0 H = 0.01$ T. No thermal hysteresis is observed between the zero-field-cooled (ZFC) and field-cooled (FC) cycles, ruling out the presence of inhomogeneous magnetism. The high- T paramagnetic state between $T = 150$ – 300 K is well described by the Curie-Weiss law $\chi(T) \sim C/(T - \Theta)$ as shown in the $1/\chi(T)$ plot (see the red solid line in the inset of Fig. 4). The fitting yields the Curie constant $C = 1.24 \pm 0.02$ cm³ K/mol and the Weiss temperature $\Theta = -38.7 \pm 0.8$ K. The negative Θ value indicates antiferromagnetic couplings between the Ni^{2+} spins. An effective magnetic moment of $\mu_{\text{eff}} = 3.15 \pm 0.02$ μ_B per Ni^{2+} calculated from the Curie constant is larger than the expected spin-only value of $\mu_{\text{cal}} = 2.83$ μ_B for $S = 1$ and $g = 2$. Here, μ_B is the Bohr magneton. Yet, it is consistent with most Ni-based compounds having sizable orbital contribution [13,21]. $\chi(T)$ exhibits a broad maximum around 38 K, and falls steeply to zero, and then shows a Curie-tail like upturn below 4 K.

The total $\chi(T)$ includes the temperature-independent terms due to Van Vleck paramagnetic χ^{VV} and core diamagnetic χ^{dia} contributions, the paramagnetic impurity contribution

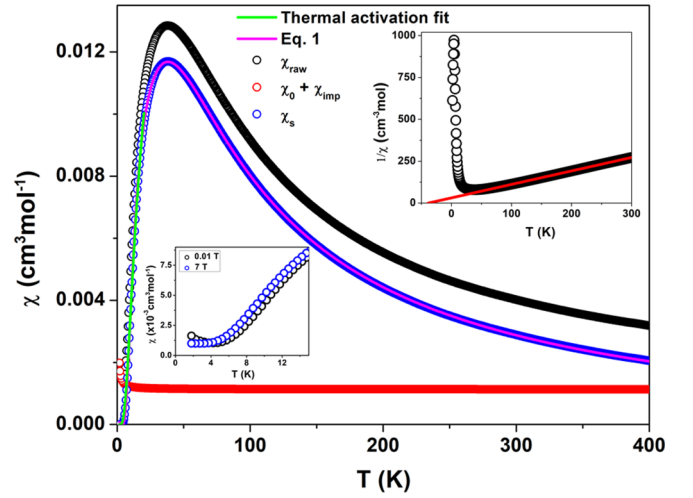


FIG. 4. The dc magnetic susceptibilities $\chi(T)$ of the $\text{K}_2\text{Ni}(\text{MoO}_4)_2$ powder sample measured in an applied field of $\mu_0 H = 0.01$ T. The black, red, and blue circles represent the raw $\chi(T)$, impurity and T -independent contribution to $\chi(T)$, and intrinsic spin dimer $\chi(T)$, respectively. The pink line is a fit to Eq. (1) and the green line to an activation expression as described in the text. The upper inset shows the $1/\chi$ plot. The red solid line is the Curie-Weiss law fit of the $T = 150$ – 300 K data to $\chi(T) \sim C/(T - \Theta)$. The lower inset is a magnified view of the low- T $\chi(T)$ at $\mu_0 H = 0.01$ and 7 T.

of $\chi_{\text{imp}}(T) \sim C'/T$, and the intrinsic spin susceptibility $\chi_s(T)$, namely, $\chi(T) = \chi^{\text{VV}} + \chi^{\text{dia}} + \chi_{\text{imp}}(T) + \chi_s(T)$. The Van Vleck paramagnetic and core diamagnetic contributions are estimated to be $\chi_0 = \chi^{\text{VV}} + \chi^{\text{dia}} = (4.69 \pm 0.07) \times 10^{-4}$ cm³/mol. The Curie-like tail stems from orphan spins. As evident from the lower inset of Fig. 4, the application of an external field of $\mu_0 H = 7$ T leads to saturation of the impurity contribution δM in $\chi \sim (M + \delta M)/H$ by the Zeeman splitting.

To extract the intrinsic $\chi_s(T)$, we subtract both χ_0 and χ_{imp} from the total $\chi(T)$. The resulting $\chi_s(T)$ clearly shows a spin-gap behavior. With increasing temperature, an exponential-like growth of $\chi_s(T)$ suggests a thermal activation of the excited triplets from the singlet ground state (see the blue circles in Fig. 4). If interdimer coupling beyond the nearest-neighbor coupling is ignored, an isolated $S = 1$ spin-dimer model with the nearest-neighbor coupling constant J_1 is expressed as [22]

$$\chi_s(T) = \frac{2N\beta g^2 \mu_B^2 (1 + 5e^{-2\beta J_1})}{3 + e^{\beta J_1} + 5e^{-2\beta J_1}}, \quad (1)$$

where $\beta = 1/k_B T$, k_B is the Boltzmann constant, and g is the g factor. In a first approximation, we attempted to fit $\chi_s(T)$ to Eq. (1). The isolated dimer model gives a nice description with $J_1/k_B T = 37.89 \pm 0.02$ K (see the pink solid line in Fig. 4). We note that the determined J_1 value is very close to the Weiss temperature $\Theta = -38.7 \pm 0.8$ K obtained from the Curie-Weiss analysis of $\chi(T)$. Considering $\Theta \propto \sum z_i J_i$, our fitting result suggests that all terms of J_i ($i \gtrsim 2$) are negligible. To confirm this assumption, we include interdimer interactions in the calculation as an effective field γ . In a mean-field approximation of the spin dimer model, the magnetic

TABLE I. Selected refined structural parameters of synchrotron XRD pattern at 300 K and neutron powder diffraction pattern at 2 K. An asterisk (*) indicates that the isotropic thermal parameters are constrained to be identical by atom type.

	300 K	2 K
Space group: <i>Cmca</i> (No. 64)		
a (Å)	8.47618 ± 0.00005	8.45125 ± 0.00009
b (Å)	19.0473 ± 0.0001	18.9620 ± 0.0003
c (Å)	10.85018 ± 0.00008	10.8408 ± 0.0002
R_p (%)	4.82	2.68
R_{wp} (%)	7.33	3.48
R_{exp} (%)	1.69	3.33
χ^2	4.33	1.04
Ni1 (8d)		
x	0.1783 ± 0.0002	0.1773 ± 0.0002
Beq (Å ²)	0.55 ± 0.04	0.06 ± 0.06
Mo1 (8f)		
y	0.5317 ± 0.0001	0.5318 ± 0.0002
z	0.2834 ± 0.0001	0.2840 ± 0.0003
Mo2 (8f)		
y	0.3429 ± 0.0001	0.3426 ± 0.0002
z	0.4637 ± 0.0001	0.4670 ± 0.0002
*Beq (Å ²)	0.76 ± 0.02	0.06 ± 0.07
K1 (8e)		
y	0.2128 ± 0.0002	0.2152 ± 0.0003
K2 (8f)		
y	0.3684 ± 0.0002	0.3704 ± 0.0003
z	0.0687 ± 0.0003	0.0698 ± 0.0005
*Beq (Å ²)	2.04 ± 0.08	0.6 ± 0.01
O1 (8f)		
y	0.4998 ± 0.0005	0.4984 ± 0.0002
z	0.1310 ± 0.0009	0.1266 ± 0.0003
O2 (8f)		
y	0.6221 ± 0.0005	0.6235 ± 0.0002
z	0.2908 ± 0.0008	0.2919 ± 0.0004
O3 (16g)		
x	0.3362 ± 0.0008	0.3371 ± 0.0003
y	0.5002 ± 0.0004	0.4984 ± 0.0001
z	0.3644 ± 0.0006	0.3647 ± 0.0002
O4 (8f)		
y	0.2671 ± 0.0005	0.2668 ± 0.0002
z	0.5570 ± 0.0009	0.5595 ± 0.0003
O5 (8f)		
y	0.3183 ± 0.0005	0.3141 ± 0.0002
z	0.3099 ± 0.0008	0.3135 ± 0.0003
O6 (16g)		
x	0.1725 ± 0.0008	0.1769 ± 0.0003
y	0.3912 ± 0.0003	0.3914 ± 0.0001
z	0.4959 ± 0.0006	0.5021 ± 0.0003
*Beq (Å ²)	1.72 ± 0.08	0.55 ± 0.05
Ni1-Ni1 (Å)	3.023 ± 0.004	2.997 ± 0.004
Ni1-O1 (Å)	2.075 ± 0.007	2.032 ± 0.003
Ni1-O3 (Å)	1.989 ± 0.007	1.994 ± 0.003
Ni1-O6 (Å)	2.073 ± 0.006	2.060 ± 0.003
O1-Ni1-O1 (deg)	86.5 ± 0.4	85.0 ± 0.2

susceptibility is given by $\chi_{mf}(T) = \chi_s/(1 + \gamma\chi_s)$. We found $\gamma \approx 0$ (not shown here), lending further support to the validity of a nearly isolated dimer model.

Further, we analyze the thermal activation behavior of $\chi_s(T)$ in the temperature range of 1.8–20 K in terms of

a simple activation expression $\chi_s \sim \exp(-\Delta_{ac}/k_B T)$ and a spin-ladder expression $\chi(T) \sim T^{-1/2} \exp(-\Delta_{lad}/k_B T)$ [23] (see the green solid line in Fig. 4). We obtain $\Delta_{ac} = 27.4 \pm 0.3$ K and $\Delta_{lad} = 38.2 \pm 0.5$ K. Noticeably, the spin gap extracted from the spin-ladder model is nearly identical to

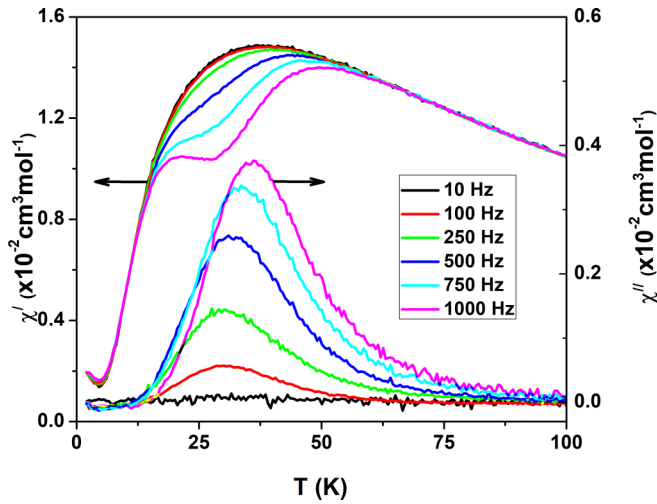


FIG. 5. Real (χ') and imaginary components (χ'') of the ac magnetic susceptibility for $\text{K}_2\text{Ni}(\text{MoO}_4)_2$ powder sample measured with an oscillating field of $H_{ac} = 1$ Oe at various frequencies of 10–1000 Hz.

the J_1 value obtained from the isolated dimer model. The simple activation model underestimates the actual spin gap. The perfect agreement among J_1 , Θ , and Δ suggests that $\text{K}_2\text{Ni}(\text{MoO}_4)_2$ could be viewed as a pure dimer system with negligible interdimer couplings and behaves like a two-leg spin ladder system. In fact, if we rotate the spin dimers (rungs), shown in Fig. 1(a), by 90° , it would be topologically equivalent to the two-leg spin ladder [24].

C. ac magnetic susceptibility

The ac magnetic susceptibility was measured with an oscillating field of $H_{ac} = 1$ Oe in various frequencies $f = 10$ –1000 Hz without applying a static magnetic field. At low frequencies $f = 10$ –250 Hz, as shown in Fig. 5, the real part of the ac magnetic susceptibility $\chi'(T)$ shows a broad maximum around 38 K, which coincides with $\chi_s(T)$ (see Fig. 4). Remarkably, with increasing frequencies from $f = 100$ Hz up to 1000 Hz (instrument upper limit), a dip feature starts to develop in $\chi'(T)$ around the spin gap of ~ 38 K, leading to a double-peak structure. This is accompanied by the growing absorption peak in $\chi''(T)$, which becomes apparent above 100 Hz. The peak of $\chi''(T)$ shifts from 30 K at 37 K with increasing frequency from 100 Hz to 1000 Hz.

As $\text{K}_2\text{Ni}(\text{MoO}_4)_2$ does not exhibit any magnetic transition or spin glass, we expect no energy dissipation driven by the ac field as other quantum paramagnets. Noteworthy is that the χ' and χ'' anomalies occurring at the spin-gap temperature indicate that the energy dissipation process is related to the singlet-triplet excitations. We recall that the 2D frustrated spin-dimer compound $\text{SrCu}_2(\text{BO}_3)_2$ shows a double-peak suppression of thermal conductivity, which is attributed to resonant scattering of phonons by the singlet-triplet excitations [25]. In this light, a dissipation channel might be activated by a similar mechanism, namely, a phonon coupling to the spin gap. Further investigations are needed to confirm this scenario.

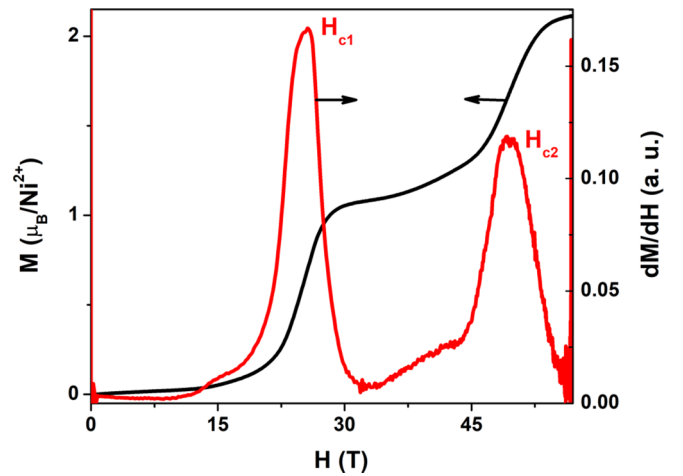


FIG. 6. High-field magnetization curve taken with a pulsed-field magnet at $T = 1.5$ K for $\text{K}_2\text{Ni}(\text{MoO}_4)_2$ powder sample. The derivative dM/dH of the magnetization shows two peaks at $\mu_0 H_{c1} \sim 25$ T and $\mu_0 H_{c2} \sim 50$ T, corresponding to magnetization plateaus.

D. High-field magnetization

We measured a high-field magnetization process at $T = 1.5$ K with a pulsed-field magnet up to 60 T. The magnetic moment was sensed with an induction method using a pickup coil device during the 25 ms pulse duration. The recorded magnetization curve $M(H)$ and its derivative dM/dH are plotted together in Fig. 6.

We observe two magnetization plateaus at $\mu_0 H_{c1} \sim 25$ T and $\mu_0 H_{c2} \sim 50$ T. Since the saturation magnetization of $\sim 2 \mu_B$ per Ni^{2+} ion is reached for fields above 50 T, the first plateau at $\mu_0 H_{c1}$ corresponds to half of the saturation magnetization. A close look unveils that the edges of the plateaus are rounded and have a finite slope due to the finite-temperature effect and magnetic anisotropy, and g -factor anisotropy. The appearance of the magnetization plateaus can be naturally understood in terms of the $S = 1$ spin-dimer model. The half plateau arises from a level crossing of the singlet ground state $|S_{\text{tot}} = 0, S_z = 0\rangle$ with the lowest triplet state $|1, -1\rangle$, while the full plateau corresponds to a level crossing of the $|1, -1\rangle$ state to the quintet $|2, -2\rangle$ state. Overall, these level crossings lead to a steplike behavior in the high-field magnetization. From the critical field $\mu_0 H_{c1} \sim 25$ T, we can estimate the zero-field gap Δ_{mag} as $\Delta_{\text{mag}}/k_B = g\mu_B H_{c1}/k_B = 38.1$ K, which agrees perfectly with the spin gap evaluated from $\chi_s(T)$. We mention that similar half-magnetization plateaus have been observed in the $S = 1$ organic chain compounds [26,27] and the inorganic $S = 1$ isolated dimer system of $\text{Ba}_3\text{Mn}_2\text{O}_8$ [22,28].

E. Specific heat

Specific heat C_p of the powder sample in zero field is presented in Fig. 7. The measured total specific heat consists of electronic, magnetic, and phonon contributions as $C_p = C_p^{\text{el}} + C_p^{\text{m}} + C_p^{\text{ph}}$. Since $\text{K}_2\text{Ni}(\text{MoO}_4)_2$ is a magnetic insulator, we assume $C_p^{\text{el}} \approx 0$. Because of the spin dimerization, the conventional approach of extracting the β value from the low- T approximation $C_p/T \sim \beta T^2$ becomes invalid. Instead, we

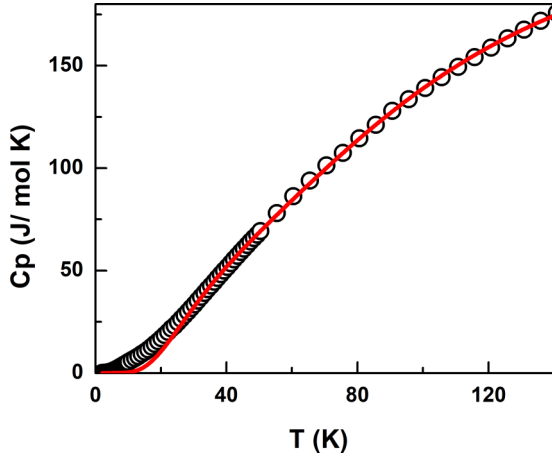


FIG. 7. The temperature dependence of specific heat $C_p(T)$ for $\text{K}_2\text{Ni}(\text{MoO}_4)_2$ measured at zero field. The red solid line is the fit to Eq. (2) to evaluate a phonon contribution.

estimate the $C_p^{\text{ph}}(T)$ contribution using the formula comprising a linear combination of the Debye and Einstein models [29] as

$$C_p^{\text{ph}}(T) = C_D \left[9k_B \left(\frac{T}{\theta_D} \right)^3 \int_0^{x_D} \frac{x^4 e^x}{(e^x - 1)^2} dx \right] + C_E \left[3R \left(\frac{\theta_E}{T} \right)^2 \frac{\exp(\frac{\theta_E}{T})}{[\exp(\frac{\theta_E}{T}) - 1]^2} \right], \quad (2)$$

where R is the universal gas constant, and θ_D and θ_E are the Debye and Einstein temperature, respectively. We note that the fitting temperature range of 50–140 K is higher than the spin-gap value of $\Delta \sim 38$ K. As shown in the red line of Fig. 7, we find a nice description of the high- T C_p with the fitting parameters $C_D = 0.72 \pm 0.01$, $C_E = 0.03 \pm 0.01$, $\theta_D = 438 \pm 6$ K, and $\theta_E = 113 \pm 2$ K.

The magnetic contribution $C_p^m(T)$ is evaluated by subtracting the estimated C_p^{ph} from the total C_p . The resulting $C_p^m(T)$

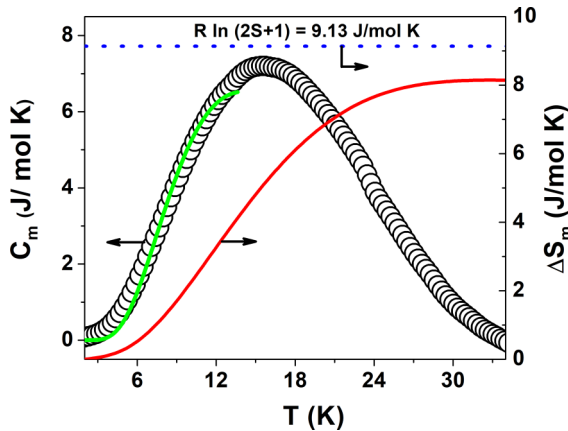


FIG. 8. Magnetic specific heat $C_m(T)$ vs T for $\text{K}_2\text{Ni}(\text{MoO}_4)_2$. The green line is a fit of the low- T $C_m(T)$ data to Eq. (3) as discussed in the text. A change in magnetic entropy ΔS_m from 2 to 34 K is obtained from the integration of the C_m/T data.

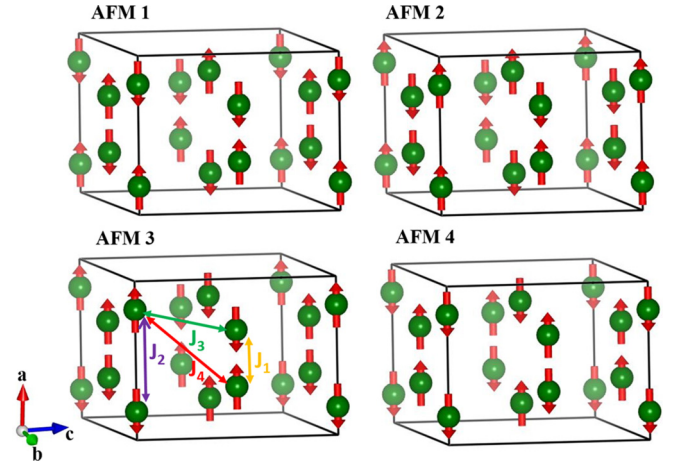


FIG. 9. Schematic representation of the spin arrangements of AFM configuration of $\text{K}_2\text{Ni}(\text{MoO}_4)_2$. The exchange parameters are denoted by different color arrows as discussed in Table III.

vs T is plotted in Fig. 8. The low- T $C_p^m(T)$ is fitted to the following expression for localized gapped excitations [30]:

$$C = \frac{nR(\Delta_{\text{sh}}/T)^2 e^{-\Delta_{\text{sh}}/T}}{(1 + ne^{-\Delta_{\text{sh}}/T})^2}, \quad (3)$$

where n is the number of excited states per spin dimer. As evident from the green line of Fig. 8, this low- T formula yields the best fit with $n = 2.08 \pm 0.04$ and $\Delta_{\text{sh}} = 37.7 \pm 0.4$ K. We find that the evaluated spin gap perfectly agrees with the values estimated from both $M(H)$ and $\chi_s(T)$. In addition, n amounts to $2/3$ of $n = 3$ expected for the triplets. The lacking triplet contribution may be because the triplets whose excitation gap is larger than $\Delta_{\text{sh}} = 37.7 \pm 0.4$ K are not properly taken into account in the fitting T range.

In addition, we evaluate the change in magnetic entropy (ΔS_m) by integrating $\int \frac{C_p^m}{T} dT$ between 2 and 34 K as shown in Fig. 8. The released magnetic entropy at 34 K is about $8.14 \text{ J mol}^{-1} \text{ K}^{-1}$, which amounts to $\sim 89.15\%$ of the total spin entropy of $R \ln(2S + 1) = 9.13 \text{ J mol}^{-1} \text{ K}^{-1}$ for a $S = 1$ spin system. This analysis suggests that the magnetic entropy is mostly released through the $S = 1$ spin dimerization process.

F. Calculated spin structure

In order to find the magnetic ground state of $\text{K}_2\text{Ni}(\text{MoO}_4)_2$, we consider several possible magnetic configurations within the unit cell, as shown in Fig. 9. The

TABLE II. The calculated total energy ΔE (relative to the total energy of FM configuration $E_{\text{FM}} = -90.7549 \text{ eV/f.u.}$), magnetic moment of Ni atom m_s^{Ni} (μ_B/atom).

Configuration	ΔE (meV/f.u.)	m_s^{Ni} (μ_B/atom)
FM	0.0	1.77
AFM1	-3.48	1.77
AFM2	-1.75	1.77
AFM3	-3.63	1.77
AFM4	-0.005	1.77

TABLE III. The calculated exchange interaction parameters (in K) as outlined in Fig. 9.

J_{ij}	Ni-Ni (Å)	Bond color	Value (K)
J_1	3.0217	Yellow	-10.01
J_2	5.4472	Violet	-0.52
J_3	5.5542	Green	-0.28
J_4	6.8780	Red	0.16

total energy per formula unit (f.u.) of FM configuration is calculated as -90.7549 eV, and ΔE 's for AFM configurations relative to the FM state are presented in Table II. Among the three considered AFM configurations, AFM3 has the lowest total energy with spin structure AFM coupled 1D chains along the a axis.

To find out the corresponding values of exchange couplings J_i within a Heisenberg model, as indicated in Fig. 9, the Hamiltonian can be expressed as $H = E_0 - \sum_{i,j} J_{ij} \sigma_i \sigma_j$, where E_0 is the total energy for all spin-independent interactions, J_{ij} is the exchange interaction parameter between the Ni^{2+} atoms at sites i and j , σ_i and σ_j are the unit vectors representing the direction of the local magnetic moment at site i and j , respectively. By solving the set of equations $E_{\text{FM}} = E_0 - 2J_1 - 2J_2 - 4J_3 - 4J_4$, $E_{\text{AFM1}} = E_0 + 2J_1 + 2J_2 - 4J_3 + 4J_4$, $E_{\text{AFM2}} = E_0 - 2J_1 - 2J_2 + 4J_3 + 4J_4$, $E_{\text{AFM3}} = E_0 + 2J_1 + 2J_2 + 4J_3 - 4J_4$, $E_{\text{AFM4}} = E_0 - 2J_1 + 2J_2$, the obtained J_i 's for AFM3 are summarized in Table III, where a negative J represents AFM interaction. The calculated $J_1 = -10.01$ K is more than 20 times larger than all other couplings including the interdimer coupling $J_2 = -0.52$ K along the chain direction (a axis), which agrees with the dimerized ground state configuration of

$\text{K}_2\text{Ni}(\text{MoO}_4)_2$ consistently. As such, we can ignore all other coupling beyond the singlet state of the dimer in the $T \rightarrow 0$ limit.

The calculated band structure and density of states (DOS) for the AFM3 spin configuration are shown in Fig. 10, which indicates a large band gap of ~ 3.8 eV between the valence and conduction bands for $\text{K}_2\text{Ni}(\text{MoO}_4)_2$ as an insulator. In addition, analysis of the site-resolved density of states reveals that the valence band is mainly composed of Mo- d and O- p states, whereas the conduction band is dominated by the Mo- d states.

G. Comparison between $\text{Ba}_3\text{Mn}_2\text{O}_8$ and $\text{K}_2\text{Ni}(\text{MoO}_4)_2$

It is inspiring to compare the $S = 1$ isolated dimer systems between $\text{Ba}_3\text{Mn}_2\text{O}_8$ [22,28] and $\text{K}_2\text{Ni}(\text{MoO}_4)_2$. As sketched in Fig. 11, the Mn dimers of $\text{Ba}_3\text{Mn}_2\text{O}_8$ are connected in a bilayer along the c direction to form a 2D triangular lattice. In contrast, the Ni dimers of $\text{K}_2\text{Ni}(\text{MoO}_4)_2$ are arranged in chains along the a direction, while forming a triangular lattice of the dimers. Obviously, a hexagonal lattice made of the $S = 1$ Mn dimers implies frustration in 2D. On the other hand, the Ni dimers in $\text{K}_2\text{Ni}(\text{MoO}_4)_2$ are frustrated along the chain direction. Noteworthy is that the BEC of the triplet state has been explored theoretically for $\text{Ba}_3\text{Mn}_2\text{O}_8$ [28]. Considering that the $S = 1$ Mn- and Ni-based dimer compounds share a triangular lattice and a half-magnetization plateau, we expect the occurrence of the BEC of triplons right above $\mu_0 H_{c1} = 25$ T, which should be addressed in a future study.

IV. CONCLUSIONS

In conclusion, we have successfully grown single crystals of $\text{K}_2\text{Ni}(\text{MoO}_4)_2$, which comprises a layered spin-1 dimer

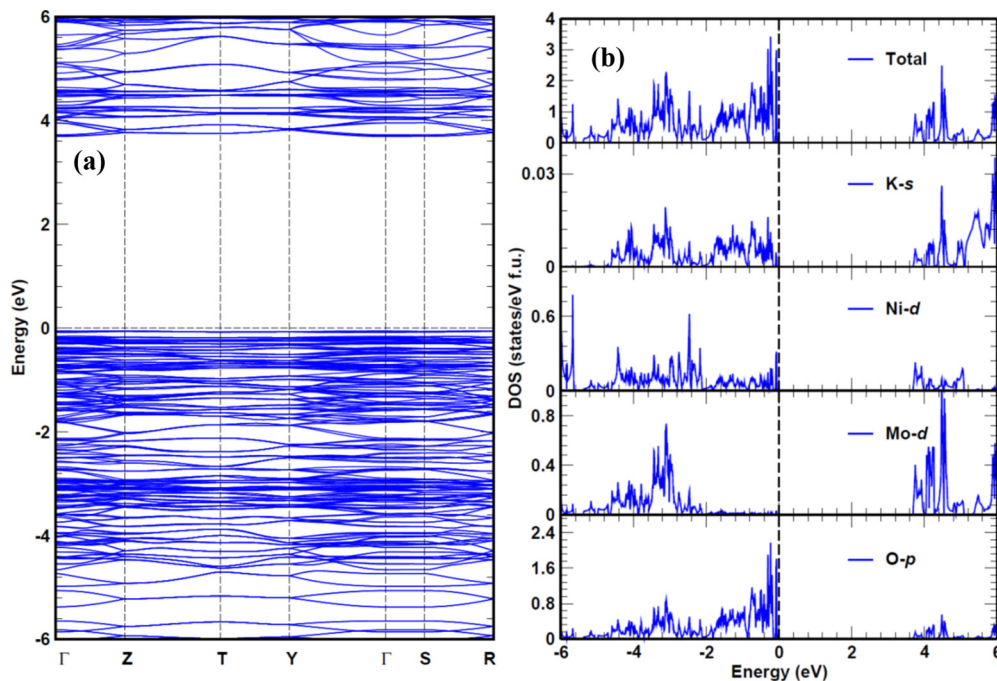


FIG. 10. (a) Electronic band structure and (b) density of states for the AFM3 configuration of $\text{K}_2\text{Ni}(\text{MoO}_4)_2$. The top of the valence band is set to zero.

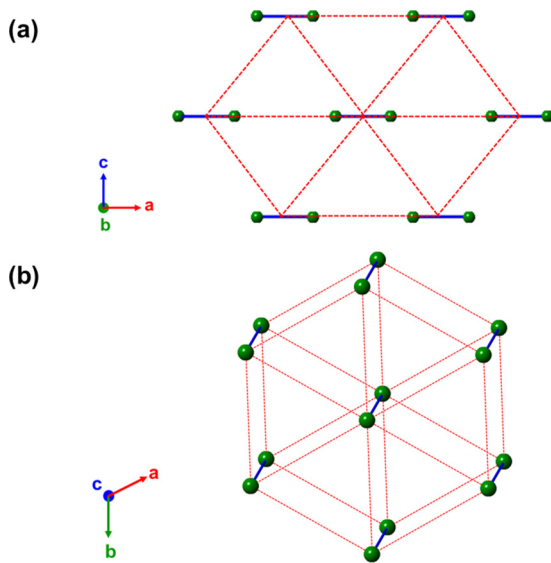


FIG. 11. The isolated dimer models for (a) $\text{K}_2\text{Ni}(\text{MoO}_4)_2$ and (b) $\text{Ba}_3\text{Mn}_2\text{O}_8$ are compared. $\text{K}_2\text{Ni}(\text{MoO}_4)_2$ has the Ni dimers being arranged along the a direction with weak interdimer frustration between the chains, and $\text{Ba}_3\text{Mn}_2\text{O}_8$ with Mn dimers arranged in a 2D hexagonal lattice.

system. The crystal structure and magnetic properties have been extensively investigated with synchrotron XRD, neutron powder diffraction, dc and ac susceptibility, and specific heat measurements, together with theoretical calculations. From the χ_s , $M(H)$, and C_m data, we determine a spin gap $\Delta/k_B \approx$

38 K. DFT calculations provide evidence that $\text{K}_2\text{Ni}(\text{MoO}_4)_2$ behaves like an almost isolated 2D $S = 1$ spin dimer, being consistent with our thermodynamic results. High-field $M(H)$ shows a half-magnetization plateau at 25 T, heralding the BEC of triplons. $\text{K}_2\text{Ni}(\text{MoO}_4)_2$ could be viewed as a rare spin system of the shortest Haldane chain in the dimer limit that may be tuned to a Haldane phase through uniaxial pressure along the a axis.

ACKNOWLEDGMENTS

G.S.M. would like to express heartfelt gratitude to Prof. F. C. Chou for all his ideas, discussions, and support. G.S.M. acknowledges support from the Ministry of Science and Technology in Taiwan under Project No. MOST 106-2119-M-002-035-MY3. R.S. acknowledges financial support provided by the Ministry of Science and Technology in Taiwan under Project No. MOST 108-2112-M-001-049-MY2. I.P.M. thanks the Department of Science and Technology in India for the support of INSPIRE Faculty Award No. DST/INSPIRE/04/2016/002275 (IFA16-PH171). K.-Y.C. was supported by the National Research Foundation (NRF) of Korea (Grant No. 2020R1A2C3012367). The synchrotron experiment was supported by NSRRC, Taiwan, with Proposal No. 2017-3-298. The neutron experiments were assisted by Dr. Shinichiro Yano and Dr. Chin-Wei Wang, and supported by NSRRC with Proposal No. N-2018-R-016 and the Australian Nuclear Science and Technology Organisation (ANSTO) with Proposals No. 7172 and No. 7239. We acknowledge the support of the HLD at HZDR, a member of the European Magnetic Field Laboratory (EMFL).

-
- [1] V. Zapf, M. Jaime, and C. D. Batista, *Rev. Mod. Phys.* **86**, 563 (2014); **86**, 1453(E) (2014).
- [2] T. Giamarchi, Ch. Rüegg, and O. Tchernyshyov, *Nat. Phys.* **4**, 198 (2008).
- [3] H. Kageyama, K. Yoshimura, R. Stern, N. V. Mushnikov, K. Onizuka, M. Kato, K. Kosuge, C. P. Slichter, T. Goto, and Y. Ueda, *Phys. Rev. Lett.* **82**, 3168 (1999).
- [4] K. Kodama, M. Takigawa, M. Horvati, C. Berthier, H. Kageyama, Y. Ueda, S. Miyahara, F. Becca, and F. Mila, *Science* **298**, 395 (2002).
- [5] T. M. Rice, *Science* **298**, 760 (2002).
- [6] M. Hase, I. Terasaki, and K. Uchinokura, *Phys. Rev. Lett.* **70**, 3651 (1993).
- [7] F. D. M. Haldane, *Phys. Rev. Lett.* **50**, 1153 (1983).
- [8] W. J. L. Buyers, R. M. Morra, R. L. Armstrong, M. J. Hogan, P. Gerlach, and K. Hirakawa, *Phys. Rev. Lett.* **56**, 371 (1986).
- [9] G. Xu, J. F. DiTusa, T. Ito, K. Oka, H. Takagi, C. Broholm, and G. Aeppli, *Phys. Rev. B* **54**, R6827 (1996).
- [10] Y. Uchiyama, Y. Sasago, I. Tsukada, K. Uchinokura, A. Zheludev, T. Hayashi, N. Miura, and P. Böni, *Phys. Rev. Lett.* **83**, 632 (1999).
- [11] A. K. Bera, B. Lake, A. T. M. N. Islam, B. Klemke, E. Faulhaber, and J. M. Law, *Phys. Rev. B* **87**, 224423 (2013).
- [12] R. M. Morra, W. J. L. Buyers, R. L. Armstrong, and K. Hirakawa, *Phys. Rev. B* **38**, 543 (1988).
- [13] B. Koteswararao, P. Khuntia, R. Kumar, A. V. Mahajan, Arvind Yogi, M. Baenitz, Y. Skourski, and F. C. Chou, *Phys. Rev. B* **95**, 180407(R) (2017).
- [14] J. P. Perdew, K. Burke, and M. Ernzerhof, *Phys. Rev. Lett.* **77**, 3865 (1996).
- [15] S. L. Dudarev, G. A. Botton, S. Y. Savrasov, C. J. Humphreys, and A. P. Sutton, *Phys. Rev. B* **57**, 1505 (1998).
- [16] G. Kresse and D. Joubert, *Phys. Rev. B* **59**, 1758 (1999).
- [17] G. Kresse and J. Hafner, *Phys. Rev. B* **47**, 558 (1993).
- [18] G. Kresse and J. Hafner, *Phys. Rev. B* **49**, 14251 (1994).
- [19] G. Kresse and J. Furthmüller, *Comput. Mater. Sci.* **6**, 15 (1996).
- [20] R. F. Klevtsova and P. V. Klevtsov, *Kristallografiya* **23**, 261 (1978).
- [21] A. Yogi, A. K. Bera, A. Maurya, R. Kulkarni, S. M. Yusuf, A. Hoser, A. A. Tsirlin, and A. Thamizhavel, *Phys. Rev. B* **95**, 024401 (2017).
- [22] M. Uchida, H. Tanaka, H. Mitamura, F. Ishikawa, and T. Goto, *Phys. Rev. B* **66**, 054429 (2002).
- [23] M. Troyer, H. Tsunetsugu, and D. Wurtz, *Phys. Rev. B* **50**, 13515 (1994).
- [24] M. Azuma, Z. Hiroi, M. Takano, K. Ishida, and Y. Kitaoka, *Phys. Rev. Lett.* **73**, 3463 (1994).
- [25] M. Hofmann, T. Lorenz, G. S. Uhrig, H. Kierspel, O. Zabara, A. Freimuth, H. Kageyama, and Y. Ueda, *Phys. Rev. Lett.* **87**, 047202 (2001).

- [26] Y. Narumi, M. Hagiwara, R. Sato, K. Kindo, H. Nakano, and M. Takahashi, *Physica B* **246-247**, 509 (1998).
- [27] Y. Narumi, K. Kindo, M. Hagiwara, H. Nakano, A. Kawaguchi, K. Okunishi, and M. Kohno, *Phys. Rev. B* **69**, 174405 (2004).
- [28] B. Xu, H.-T. Wang, and Y. Wang, *Phys. Rev. B* **77**, 014401 (2008).
- [29] B. Koteswararao, R. Kumar, P. Khuntia, Sayantika Bhowal, S. K. Panda, M. R. Rahman, A. V. Mahajan, I. Dasgupta, M. Baenitz, K. H. Kim, and F. C. Chou, *Phys. Rev. B* **90**, 035141 (2014).
- [30] H. Tsujii, B. Andraka, M. Uchida, H. Tanaka, and Y. Takano, *Phys. Rev. B* **72**, 214434 (2005).